Supporting Information

for

Multiple Interfaces Coupling Triggered Built-in Electric Field over Double-Sandwiched RGO/Cobalt silicate/Cobalt-Iron Phosphide for Improving Overall Water-Splitting Performance

Yifu Zhang[1,2,*], Xianfang Tan[1], Xiaoyu Pei[2], Yang Wang[2], Shengping Yi[3], Qiushi Wang[4,*], Xiaoming Zhu[1], Changgong Meng[2], Chi Huang[3,*]

[1]*Hubei Key Laboratory of Radiation Chemistry and Functional Materials, School of Nuclear Technology and Chemistry & Biology, Hubei University of Science and Technology, Xianning 437100, China*

[2]*School of Chemistry, Dalian University of Technology, Dalian 116024, China*

[3]*College of Chemistry and Molecular Sciences, Wuhan University, Wuhan 430072, China*

[4]*School of Physics and Materials Engineering, Dalian Minzu University, Dalian 116600, P. R. China*

*Corresponding authors.

Yifu Zhang

E-mail address: yfzhang@dlut.edu.cn

Qiushi Wang

E-mail address: wangqiushi@dlnu.edu.cn

Chi Huang

E-mail address: chihuang@whu.edu.cn

1. Experiment section

1.1. Reagents and materials

All the chemicals were used directly without any further purification. Tetraethyl orthosilicate (TEOS, $[Si(OC_2H_5)_4]$), ammonium hydroxide ($NH_3 \cdot H_2O$, 25 wt%), graphite flakes with an average diameter of 37.4 microns, sodium nitrate ($NaNO_3$), sulfuric acid (H_2SO_4, 98 wt%), potassium permanganate ($KMnO_4$), hydrogen peroxide (H_2O_2, 30%), hydrochloric acid (HCl), cetyltrimethyl ammonium bromide (CTAB), ammonia ($NH_3 \cdot H_2O$, 36.5 wt%), methyl alcohol, anhydrous ethanol, cobalt chloride ($CoCl_2 \cdot 6H_2O$), cobalt nitrate ($Co(NO_3)_2 \cdot 6H_2O$), 2-methylimidazole, ferrous sulfate ($FeSO_4 \cdot 7H_2O$), sodium hypophosphite ($NaH_2PO_2 \cdot H_2O$), acetylene black, N-methyl-2-pyrrolidone (NMP, C_5H_9NO), and polyvinylidene fluoride (PVDF, $-(CH_2-CF_2)_n-$) were purchased from Sinopharm Chemical Reagent Co., Ltd.

1.2. Synthesis of the precursor sandwich-like rGO/CS

The synthesis of the precursor sandwich-like ***reduced graphene oxide/Co_2SiO_4 (rGO/CS)*** mainly contains three steps according to our previous work [1] as following:

1.2.1. Synthesis of graphene oxide (GO)

The preparation of GO was according to a modified Hummer's method on the previous report [2], which was mainly divided into three stages: low temperature stage, medium temperature stage and high temperature stage. **Low temperature stage**: according to take 2 g graphite, 1 g $NaNO_3$, 46 mL H_2SO_4, put them in 500 mL beaker, ice bathing, ultrasonic within 15 min until the beaker of solution temperature below 3 °C, transferred them to the ice bath pot then slowly added 6 g $KMnO_4$, stirring for 1 h to get blackening solution, the edge of the solution for the dark green; **Medium temperature stage**: under the condition of 35 °C water bath mixing 1 h, the solution getting into viscous significantly. **High temperature stage**: adding in 92 mL deionized water inside the beaker, the solution into brown, in 90 °C water bath stirring for 15 min after, then pour into 300 mL deionized water, 10 mL 30% H_2O_2 in turn, stirring for 10 min after delamination, for the gold at the top, bottom was black, poured out on the yellow clear liquid and added 10 mL of the mass fraction of 10% HCl, stirring again let stand for 12 h after stratification, poured out the gold solution at the top that adding deionized water until the upper supernatant fluid yellow became not obvious at this time no longer with deionized water, the GO solution was successfully prepared and turned the solution to the brown bottle for use [2], The morphology of GO is nanosheets [3].

1.2.2. Synthesis of sandwich-like rGO/SiO_2

Sandwich-like GO/SiO_2 was prepared according to our previous work [4]. In detail, 0.15 g CTAB was added to the mixed solution contained 120 mL ethanol and 30 mL deionized water, and stirred for 5 minutes. 50 mg GO was drizzled and stirred for 10 minutes. After the GO dispersed evenly, 3 mL of $NH_3 \cdot H_2O$ (25 wt%) was added drop by drop, and then TEOS solution was added slowly to the above solution under intense stirring to obtain GO/SiO_2 after 4 h. The GO/SiO_2 is used to synthesize sandwich-like **rGO/Co_2SiO_4 (rGO/CS)**.

1.2.3. Synthesis of sandwich-like rGO/CS

In a typical synthesis, ***Solution A*** was formed by dispersing 0.08 g of GO/SiO_2 in 16 mL anhydrous ethanol for 10 minutes under ultrasound. 0.20 g of $CoCl_2 \cdot 6H_2O$ were placed in a mixture of 1.6 mL deionized water (DI) and 8 mL ammonia, respectively, and stirred evenly to form ***Solution B*** with different Co contents. ***Solution A*** was poured into ***Solution B***, while the mixed solution was stirred at room temperature for 30 minutes. Then it was transferred to 50 mL Teflon-lined steel autoclave, and reacted at 180 ℃ for 24 hours [5]. The obtained solids (rGO/CS) were washed with DI water and ethanol for several times and dried at 80 ℃ for 12 hours in a vacuum oven. The rGO/CS is used to synthesize double sandwich-like rGO/CS/Co-MOF.

1.3. Synthesis of double sandwich-like rGO/CS/Co-MOF and Co-MOF

100 mg rGO/CS, 0.2885 g $Co(NO_3)_2 \cdot 6H_2O$ were added to 15 mL methanol solution, and ultrasonic treatment was conducted for 10 minutes to form ***Solution C***. 0.6692 g 2-methylimidazole were dissolved in 15 mL methanol to form ***Solution D***. Then, ***Solution D*** was slowly added to ***Solution C*** under agitation, and ultrasonic processing was conducted at 25 ℃ for 10 minutes. Later, the mixed solution was stirred at room for 6 hours, and washed with methanol for three times. The product was vacuum dried at 70 ℃ for 12 hours to obtain rGO/CS/Co-MOF.

For comparison, the Co-MOF was synthesized using the same method of rGO/CS/Co-MOF without rGO/CS.

1.4. Synthesis of rGO/CS/Co,Fe-MOF

The iron ion exchanged rGO/CS/Co-MOF (denoted as rGO/CS/Co,Fe-MOF) was synthesized using ion-exchange method. In a typical synthesis, 9 mg $FeSO_4 \cdot 7H_2O$ were dissolved to 15 mL H_2O,

then 50 mg rGO/CS/Co-MOF and 20 mL anhydrous ethanol were added in sequence. The above solutions were reacted at 50 ℃ for 20 minutes. After that, the products were washed with water and ethanol for several times. The products were dried in vacuum at 70 ℃ for 12 hours to obtain rGO/CS/Co,Fe-MOF. The obtained rGO/CS/Co,Fe-MOF were named as **rGO/CS/Co,Fe-MOF-1, rGO/CS/Co,Fe-MOF-2 and rGO/CS/Co,Fe-MOF-3** according to 5, 9 and 13 mg $FeSO_4·7H_2O$, respectively. Among them, rGO/CS/Co,Fe-MOF-2 was selected to synthesize rGO/CS/$(Co,Fe)_xP_y$ because of its best OER performance.

1.5. Synthesis of rGO/CS/$(Co,Fe)_xP_y$

The rGO/CS/Co,Fe-MOF was phosphorized by the following step and named as rGO/CS/$(Co,Fe)_xP_y$. In a typical synthesis, 500 mg $NaH_2PO_2·H_2O$ was placed in a quartz boat (**Q1**), and 100 mg rGO/CS/Co,Fe-MOF was placed in another quartz boat (**Q2**). The above two quartz boats were placed in the same tube furnace. The quartz boat **Q1** was in the front of quartz boat **Q2** along the flow of N_2. The tube furnace was heated at 400 ℃ in N_2 atmosphere for 2 h to obtain a black solid. The obtained rGO/CS/$(Co,Fe)_xP_y$ were named as **rGO/CS/$(Co,Fe)_xP_y$-1, rGO/CS/$(Co,Fe)_xP_y$-2 and rGO/CS/$(Co,Fe)_xP_y$-3** based on the mass of 100, 500 and 1000 mg $NaH_2PO_2·H_2O$, respectively. Among them, **rGO/CS/$(Co,Fe)_xP_y$-2** showed the best OER activity in subsequent tests and was chosen as the final target sample.

1.6. Synthesis of rGO/CS/Co_xP_y and $(Co,Fe)_xP_y$

For comparison, rGO/CS/Co_xP_y and $(Co,Fe)_xP_y$ were also synthesized. The rGO/CS/Co_xP_y was synthesized using the same method of rGO/CS/$(Co,Fe)_xP_y$ using rGO/CS/Co-MOF as the precursor. The $(Fe,Co)_xP_y$ was synthesized using the Co-MOF as the precursor with the same method of rGO/CS/$(Co,Fe)_xP_y$.

1.7. Material characterizations

Field emission scanning electron microscopy (FE-SEM, NOVA NanoSEM 450, FEI) and transmission electron microscopy (TEM, FEI Tecnai F30, FEI) were used to get morphologies and structure of the samples. Energy-dispersive X-ray spectrometer (EDS) and elemental mapping were employed by scanning electron microscope (SEM, QUANTA450) to investigate elements of products. X-ray diffraction (XRD) measurement was conducted to analyze the crystalline structure and composition using a Panalytical X'Pert

powder diffractometer with Cu Kα radiation. Raman spectra were obtained using a Thermo Scientific spectrometer, at an exciting wavelength of 532 nm. Energy-dispersive Fourier transform infrared spectroscopy (FTIR) pattern of the solid samples was measured using KBr pellet technique (About 1 wt.% of the samples and 99 wt.% of KBr were mixed homogeneously, and then the mixture was pressed to a pellet) and recorded on a Nicolet 6700 spectrometer from 4000 to 400 cm^{-1} with a resolution of 4 cm^{-1}. The specific surface areas and pore structure were determined by a nitrogen adsorption-desorption analyzer (Micromeritics ASAP-2020). Prior to determination of the N_2 adsorption-desorption isotherm, the samples were degassed at 250 °C for several hours. The X-ray photoelectron spectroscopy (XPS) measurements were performed on ESCALAB 250Xi electron spectrometer. The spectra were excited using Al Kα radiation with a pass energy of 20 eV.

1.8. Fabrication of electrodes

5 mg rGO/CS/$(Co,Fe)_xP_y$, 480 μL isopropyl alcohol and 20 μL Nafion were added into a 3 mL centrifuge tube. In the following ultrasound of 30 minutes, 5 μL sample were dropped onto the surface of the glassy carbon electrode (d = 5 mm). Leaving to dry at room temperature, 20 μL were added in twice. The payload of the active substance is about 1.3 $mg \cdot cm^{-2}$.

1.9. Electrochemical characterizations

The OER properties of the working electrode were evaluated by a three-electrode system using an Hg/HgO electrode as the reference electrode and a Pt wire as the counter electrode. The linear sweep voltammetry (LSV), cyclic voltammetry (CV) and electrochemical impedance spectroscopy (EIS) measurements were performed in 1 M KOH as electrolyte on a PINE electrochemical station. The specific overpotential (mV) was calculated from the LSV curves based on the following equation:

$$E_{RHE} = E_{Hg/HgO} + 0.059 * pH + 0.098 \quad (S1)$$

$$\eta = (E_{RHE} - 1.23) * 1000 \quad (S2)$$

Where E_{RHE} denotes voltage corresponding to reversible hydrogen electrode; η (mV) represents overpotential; 0.098 signifies the standard potential of Hg/HgO reference electrode. (1 mol KOH pH 13.85)

Water splitting test was performed using a two-electrode cell. Two pieces of clean carbon felt (1 ×1 cm) were used as catalyst support. 200 μL of the above-mentioned ink was coated on the carbon felt by drop-casting method and then dried under vacuum condition (catalyst loading amount is ~2.0 mg cm^{-2}). Two

pieces of the modified carbon felt as dual working electrodes were inserted into 1.0 M KOH solution to conduct water splitting.

Figure S1

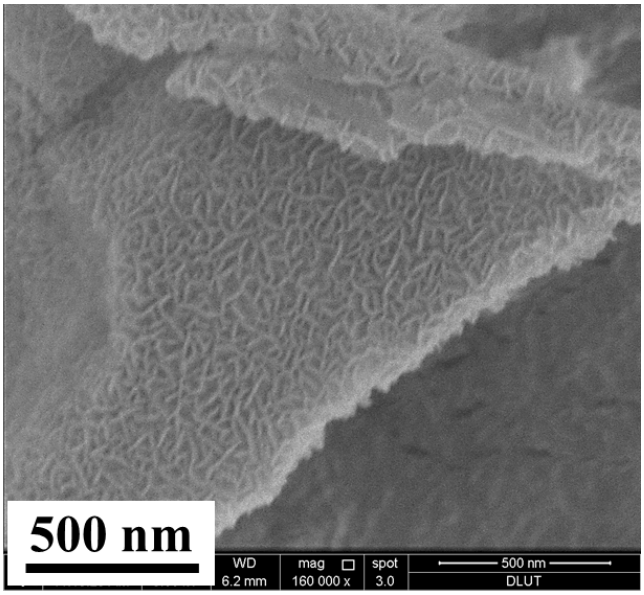

Figure S1. A SEM image of rGO/CS.

Figure S2

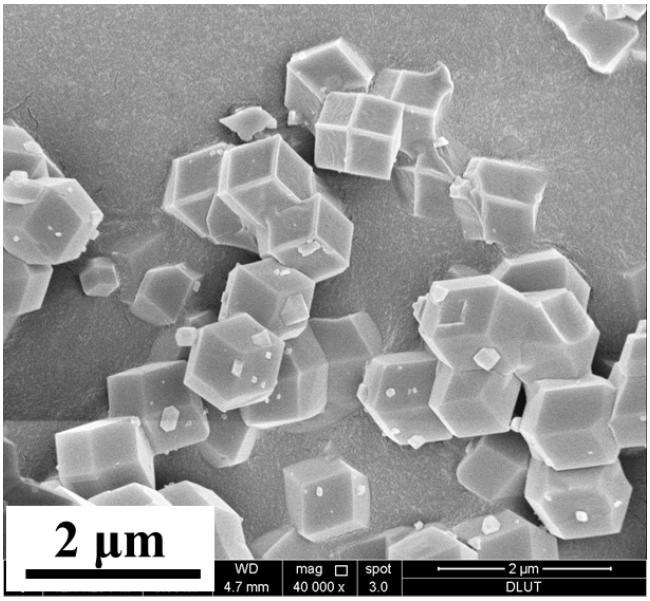

Figure S2. A SEM image of Co-MOF.

Figure S3

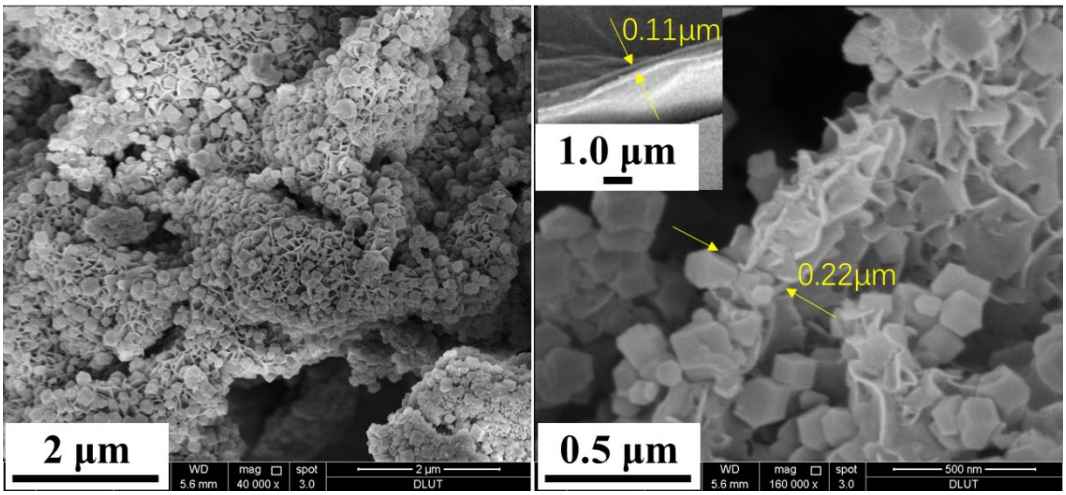

Figure S3. SEM images of rGO/CS/Co-MOF, inserting the SEM of rGO.

Figure S4

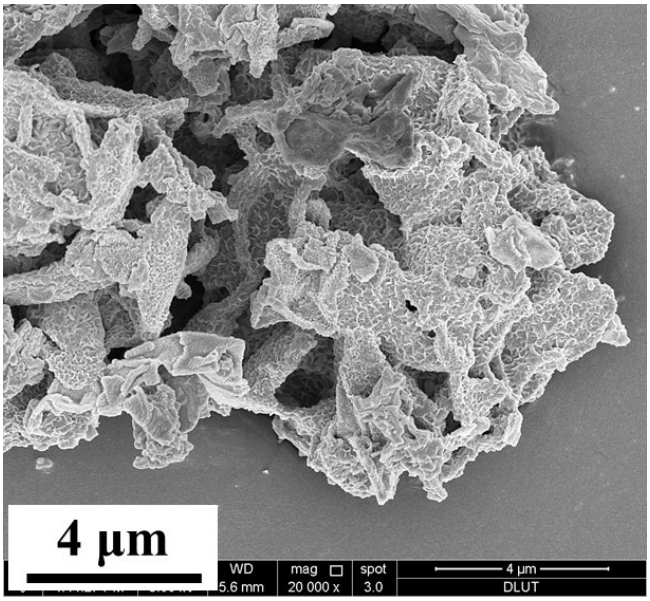

Figure S4. A SEM image of rGO/CS/$(Co,Fe)_xP_y$.

Figure S5

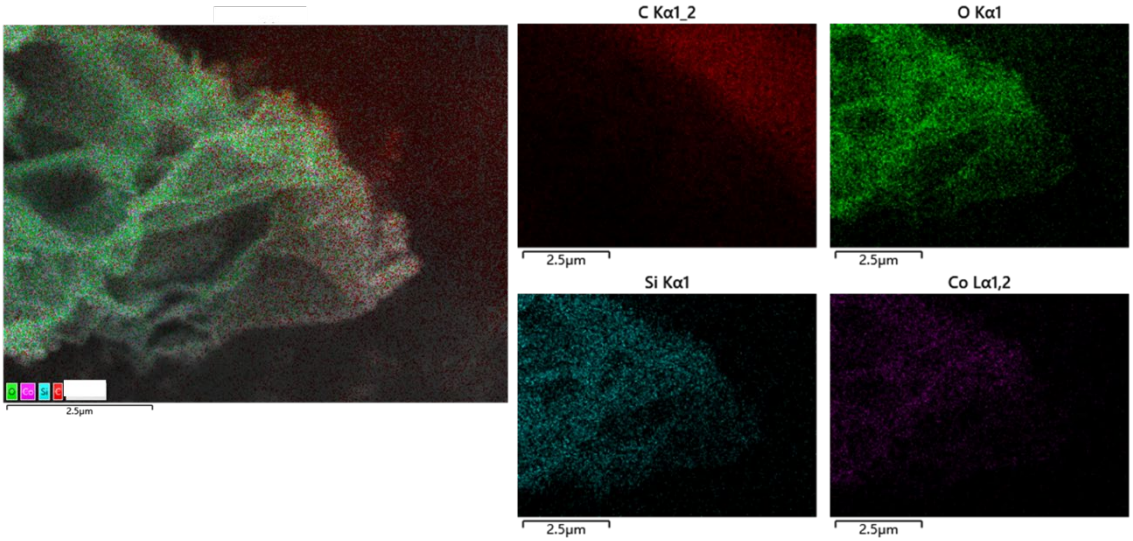

Figure S5. Elemental mapping images of rGO/CS.

Figure S6

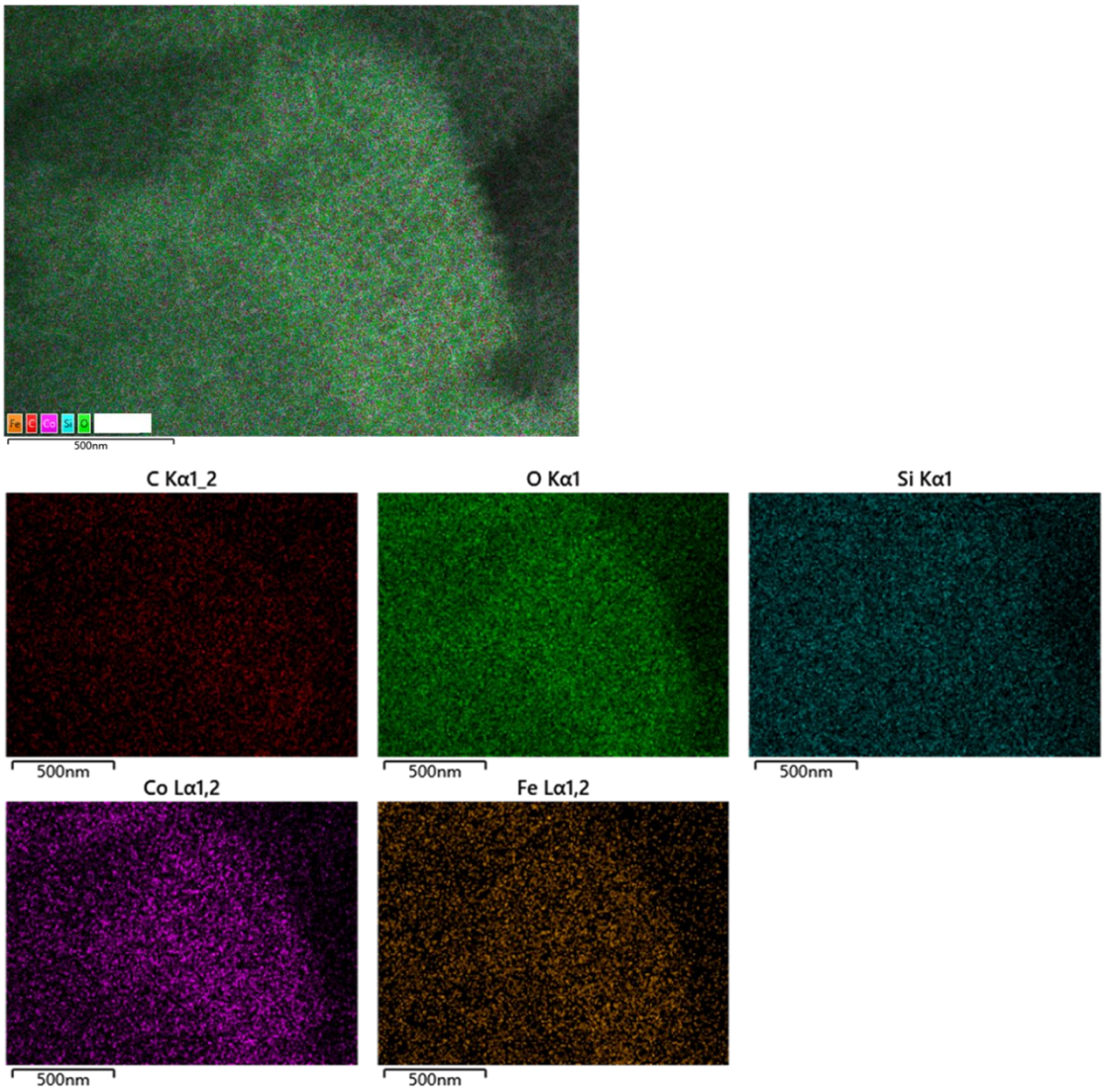

Figure S6. Elemental mapping images of rGO/CS/Co,Fe-MOF.

Figure S7

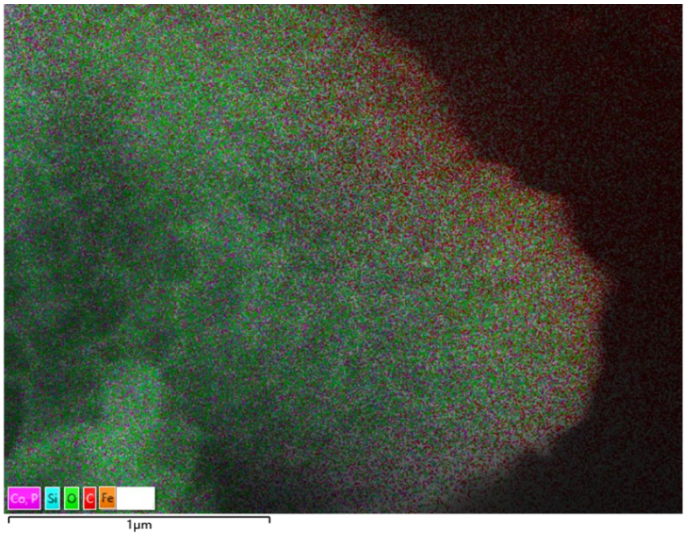

Figure S7. Elemental mapping image of rGO/CS/$(Co,Fe)_xP_y$.

Figure S8

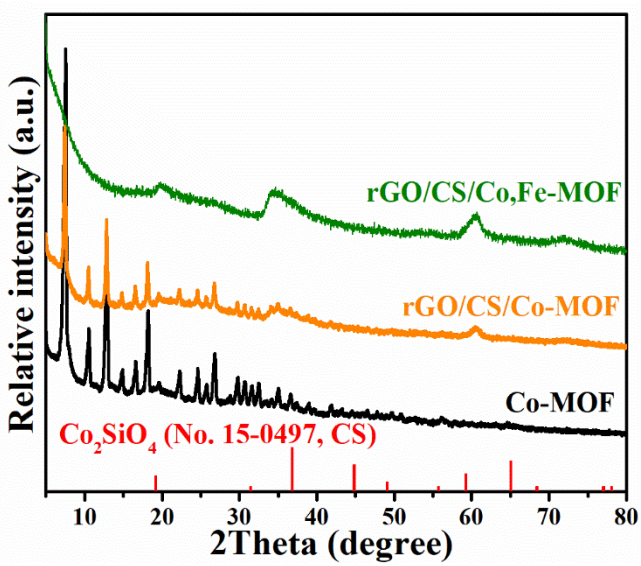

Figure S8. XRD patterns of Co-MOF, rGO/CS/Co-MOF and rGO/CS/Co,Fe-MOF.

Figure S9

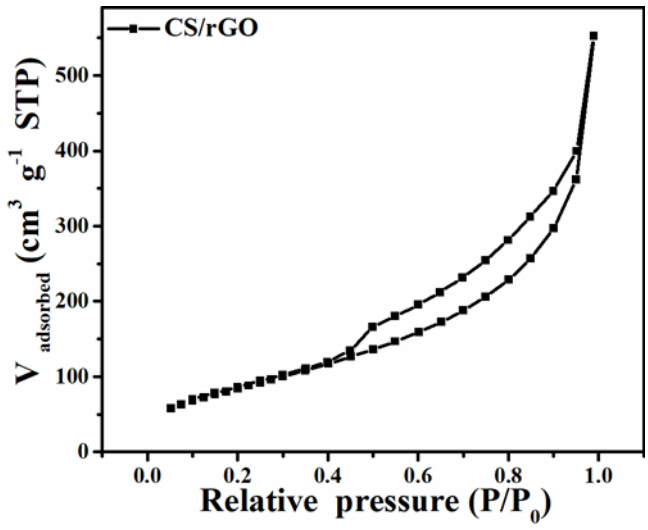

Figure S9. Nitrogen adsorption-desorption isotherms of rGO/CS.

Figure S10

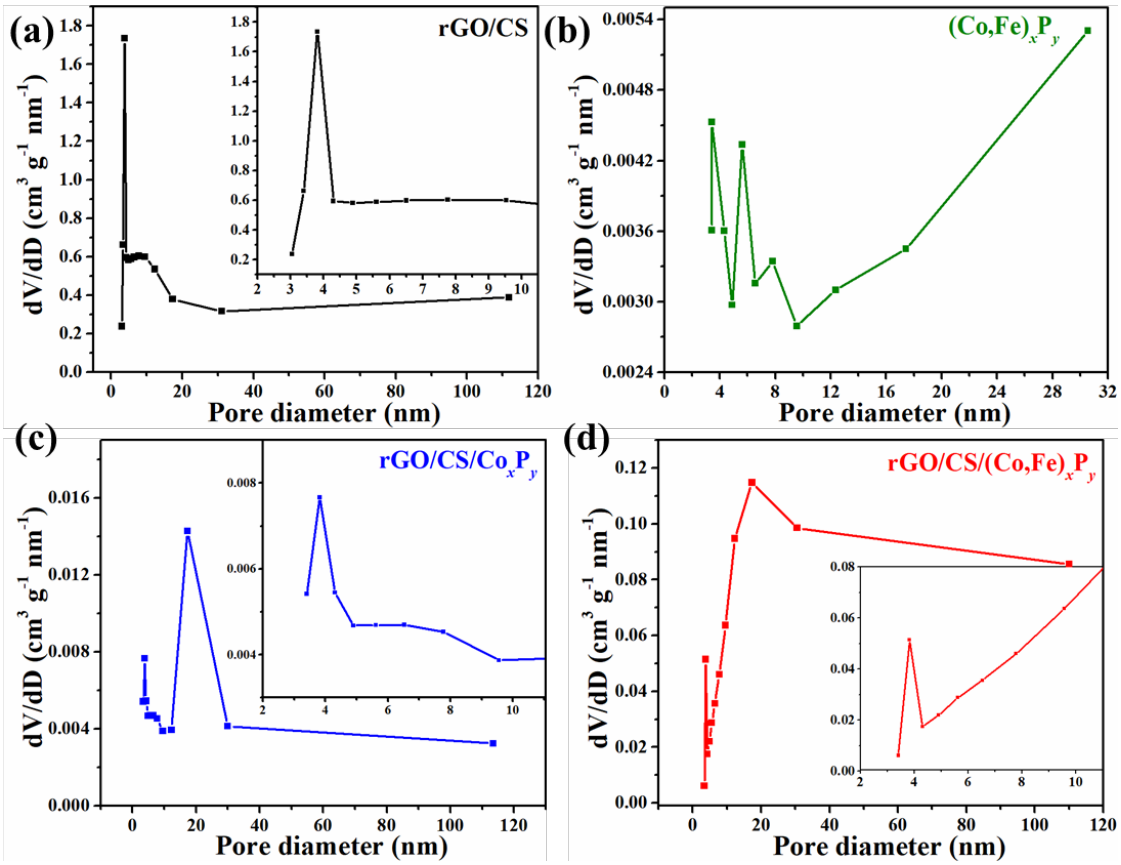

Figure S10. Pore size-distribution curves calculated by the BJH method of the samples: (a) rGO/CS, (b) $(Co,Fe)_xP_y$, (c) rGO/CS/Co_xP_y and (d) rGO/CS/$(Co,Fe)_xP_y$.

Figure S11

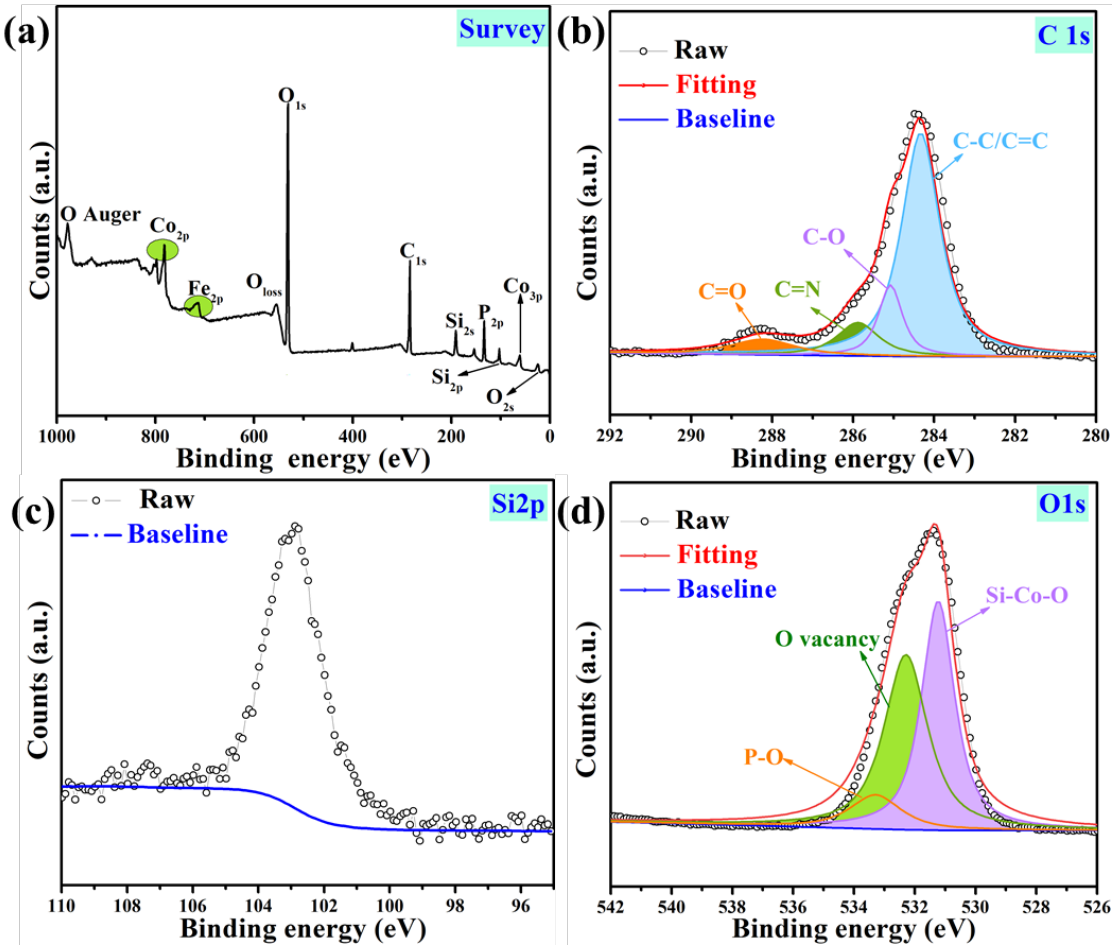

Figure S11. XPS spectra of rGO/CS/$(Co,Fe)_xP_y$: (a) Full spectrum; (b) C1s; (c) Si2p; (d) O1s.

Figure S12

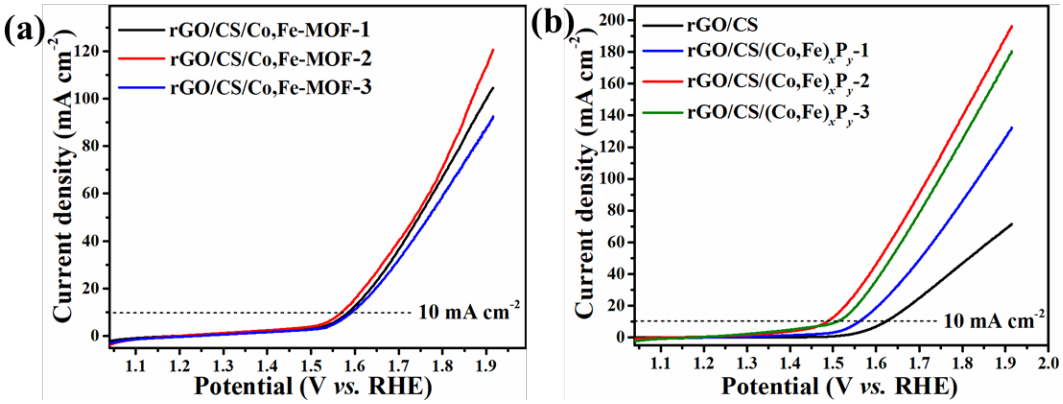

Figure S12. The electro-catalytic property of OER: (a) LSV curves of rGO/CS/Co,Fe-MOF-1, rGO/CS/Co,Fe-MOF-2 and rGO/CS/Co,Fe-MOF-3. (b) LSV curves of rGO/CS, rGO/CS/$(Co,Fe)_xP_y$-1, rGO/CS/$(Co,Fe)_xP_y$-2 and rGO/CS/$(Co,Fe)_xP_y$-3.

Figure S13

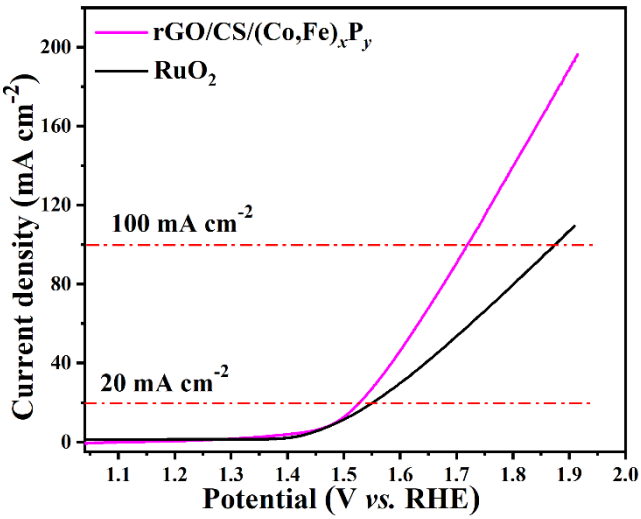

Figure S13. The electro-catalytic property of OER: LSV curves of rGO/CS/$(Co,Fe)_xP_y$ and commercial RuO_2.

Figure S14

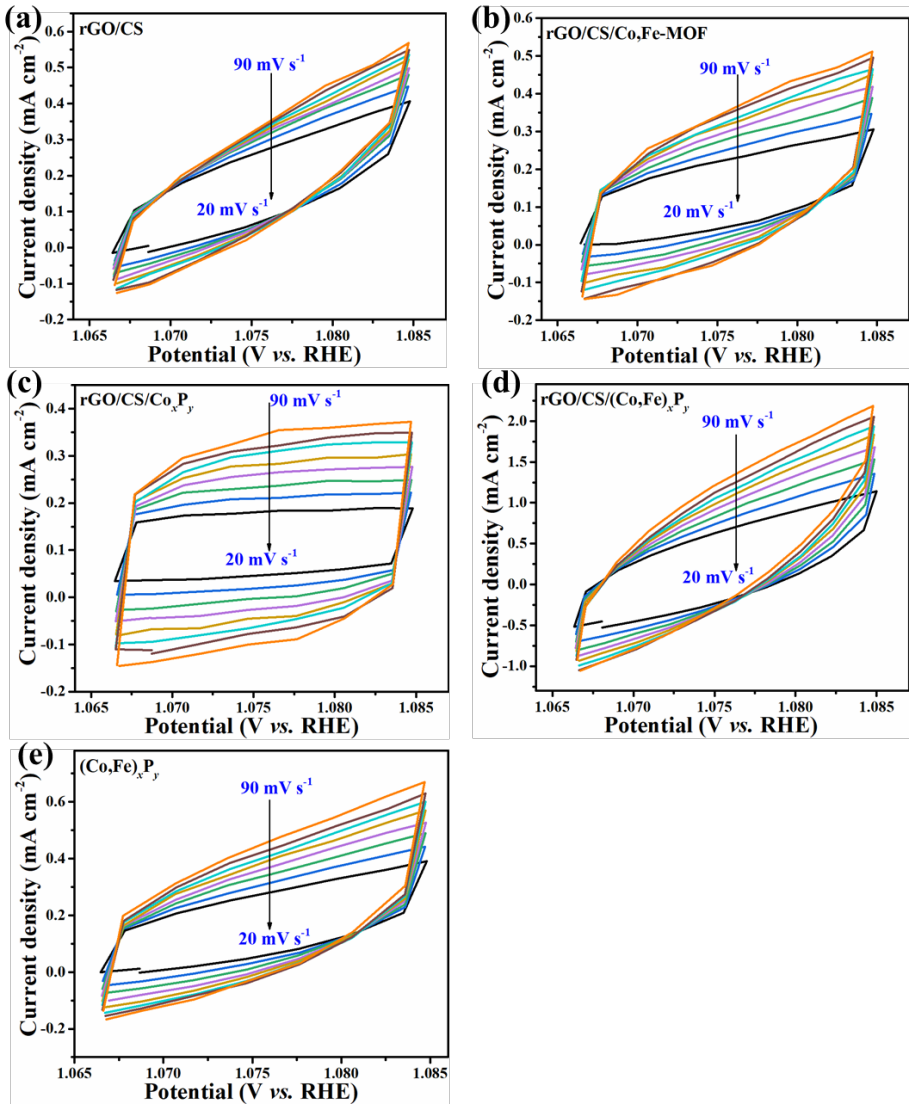

Figure S14. CV curves of (a) rGO/CS, (b) rGO/CS/Co,Fe-MOF, (c) rGO/CS/Co_xP_y, (d) rGO/CS/$(Co,Fe)_xP_y$ and (e) $(Co,Fe)_xP_y$ for OER.

Figure S15

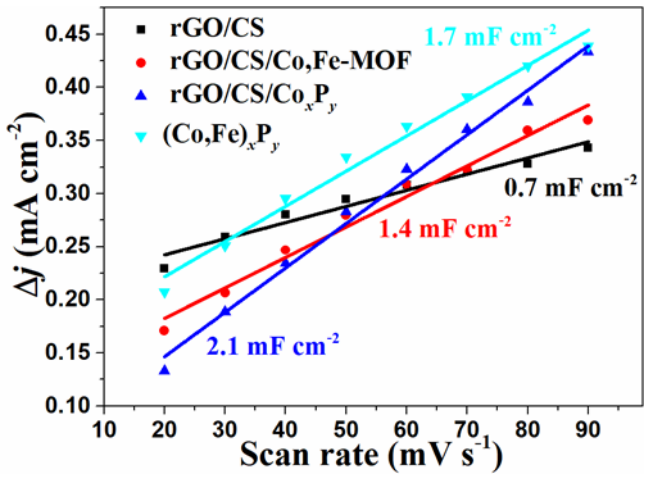

Figure S15. The enlarge figure of Figure 4d (Linear relationships of capacitive current *vs.* scan rate of rGO/CS, rGO/CS/Co,Fe-MOF, rGO/CS/Co$_x$P$_y$ and (Co,Fe)$_x$P$_y$).

Figure S16

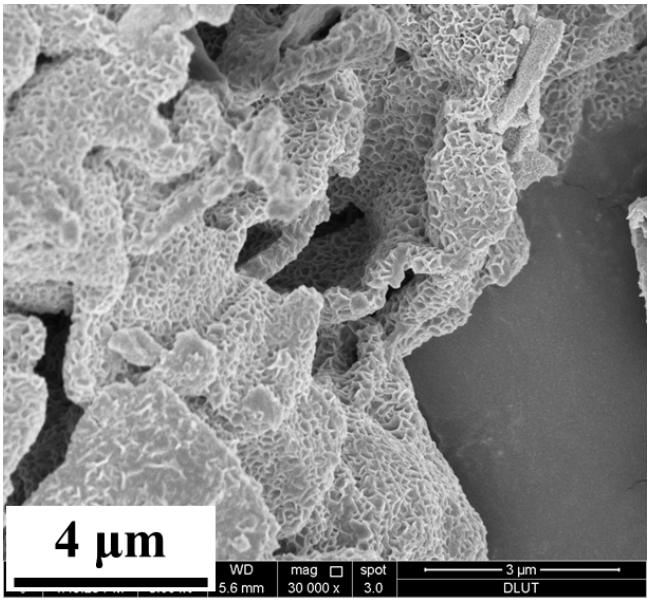

Figure S16. SEM image of rGO/CS/$(Co,Fe)_xP_y$ after long-term chronopotentiometry test at 10 mA cm^{-2}.

Figure S17

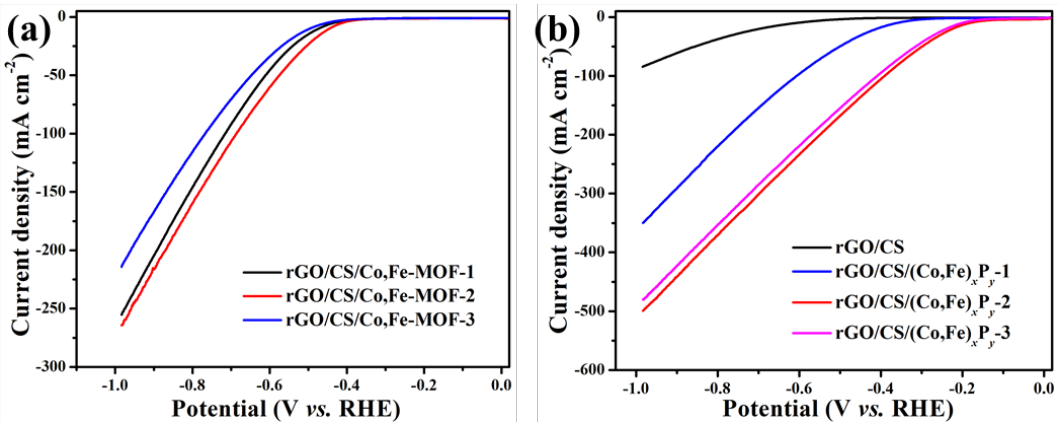

Figure S17. The electro-catalytic property of HER: (a) LSV curves of rGO/CS/Co,Fe-MOF-1, rGO/CS/Co,Fe-MOF-2 and rGO/CS/Co,Fe-MOF-3. (b) LSV curves of rGO/CS, rGO/CS/$(Co,Fe)_xP_y$-1, rGO/CS/$(Co,Fe)_xP_y$-2 and rGO/CS/$(Co,Fe)_xP_y$-3.

Figure S18

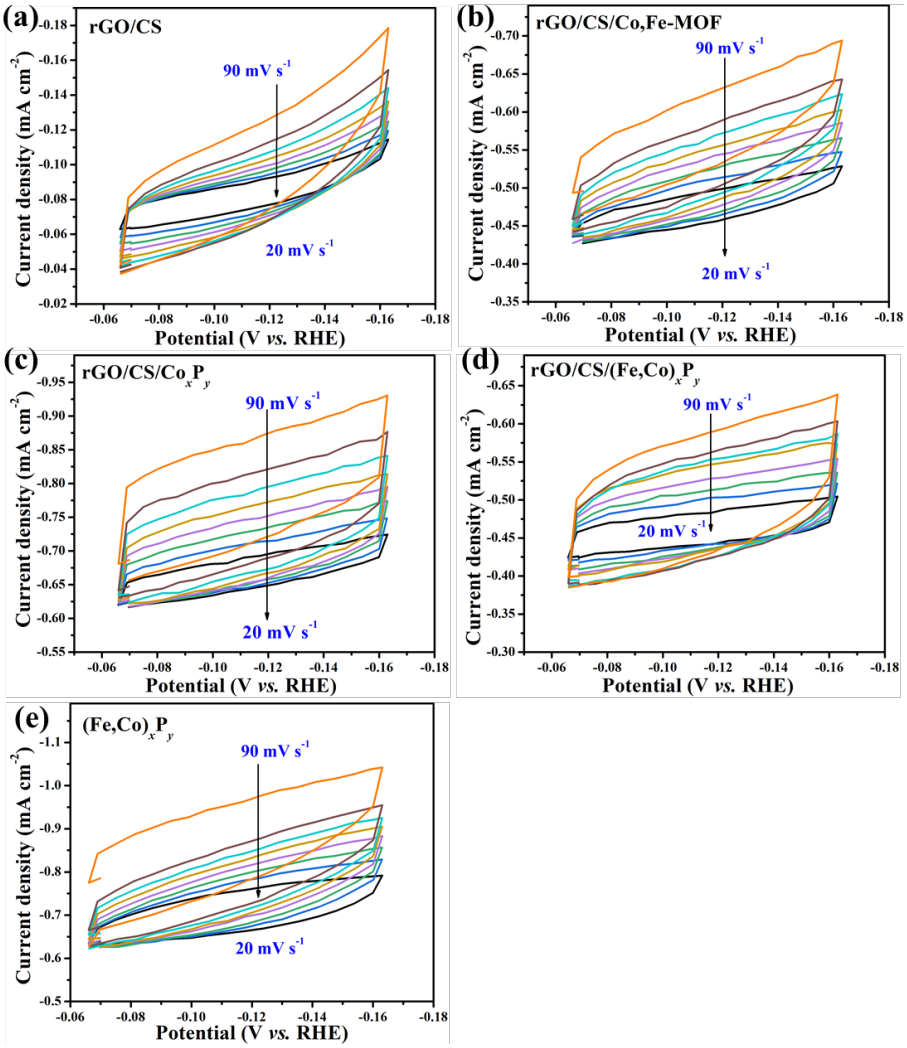

Figure S18. CV curves of (a) rGO/CS, (b) rGO/CS/Co,Fe-MOF, (c) rGO/CS/Co_xP_y, (d) rGO/CS/$(Co,Fe)_xP_y$ and (e) $(Co,Fe)_xP_y$ for HER.

Figure S19

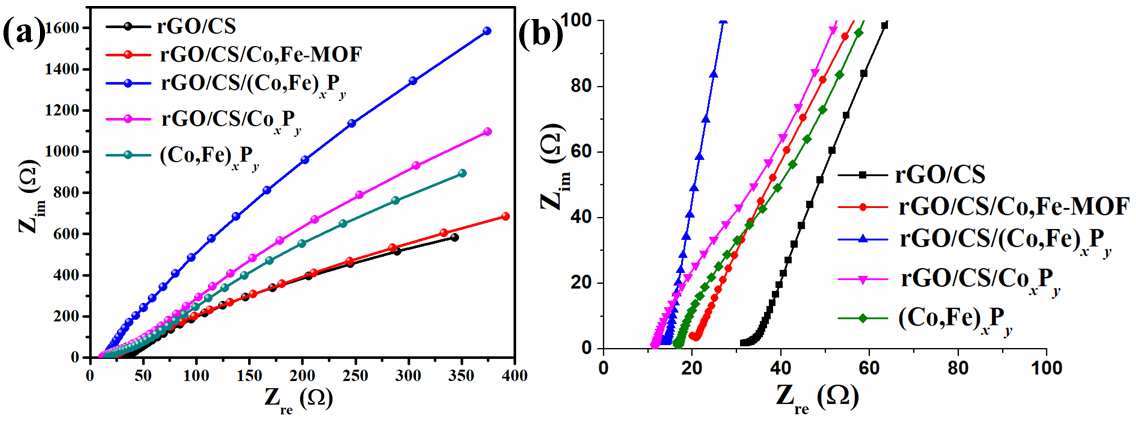

Figure S19. (a) The normal and (b) the enlarged EIS curves of rGO/CS, rGO/CS/Co,Fe-MOF, rGO/CS/$(Co,Fe)_xP_y$, rGO/CS/Co_xP_y and $(Co,Fe)_xP_y$.

Figure S20

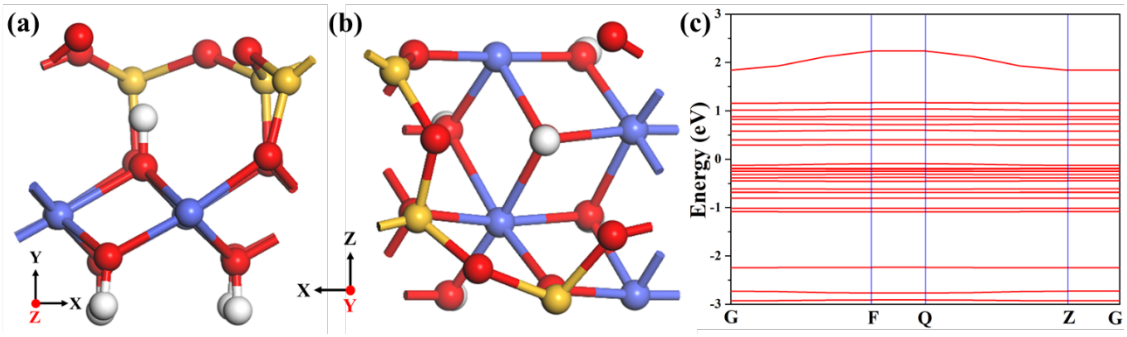

Figure S20. DFT calculations of CS: (a-b) The crystal structures of CS at different views for calculations; (c) The band structure of CS.

Figure S21

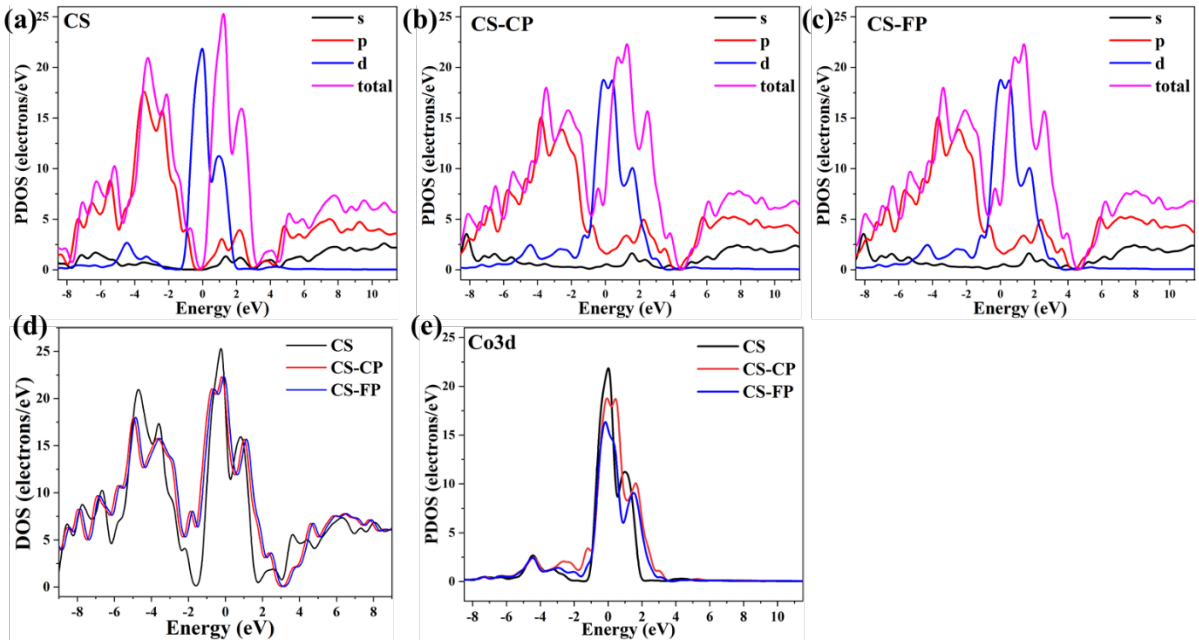

Figure S21. DFT calculations of CS, CS-CP and CS-FP: (a) DOS of CS; (b) DOS of CS-CP; (c) DOS of CS-FP; (d) The total DOS comparison; (e) The PDOS of Co3d.

Table S1

Table S1. Composition of rGO/CS/$(Co,Fe)_xP_y$ by EDS and XPS.

Elements	XPS (atom%)	EDS (wt.%)
C	31.5	34.7
O	43.2	37.2
Co	6.7	8.9
Fe	3.0	3.9
Si	5.5	5.9
P	10.1	9.4

Table S2

Table S2. OER performance of this work compared with the previously reported TMSs, transition metal oxide/hydroxide and some Co-based materials in 1.0 M KOH.

Catalysts	Loading amount (mg/cm^2)/Collector	Overpotential (mV) @10 mA/cm^2	Ref.
rGO/CS/$(Co,Fe)_xP_y$	0.63/glassy carbon	256	**This work**
CoP/CSNSs	0.51/glassy carbon	309	[6]
Fe/Fe_2O_3@Fe-N-C	0.61/glassy carbon	460	[7]
Fe_3O_4@Co_9S_8/rGO	0.25/glassy carbon	340	[8]
Fe_3O_4@$NiFe_xO_y$	2.7/spin-coat on ITO glass	420	[9]
Co_3O_4/C	0.2/grow on Cu foil	350	[10]
Reduced Co_3O_4	0.136/glassy carbon	410	[11]
Co_3O_4@BP	0.66/glassy carbon	400	[12]
CoO_x/N-GO	0.6/glassy carbon	370	[13]
$Fe_{0.5}Ni_{0.5}Co_2O_4$	--/grow on Ni foam	350	[14]
ZIF-67@$Co(OH)_2$	0.2/glassy carbon	354	[15]
α-$Co(OH)_2$	0.28/glassy carbon	380	[16]
$Co(OH)_2$@N-C	0.15/glassy carbon	360	[17]
$Co(OH)_2$@$Ni(OH)_2$/CC	--/grow on 1.0 × 2.0 cm CC	330	[18]
CeO_2/$Co(OH)_2$	--/glassy carbon	410	[19]
α-FeOOH	--/screen printed electrode	338	[20]
$Ni(OH)_2$ hollow cubes	0.2/glassy carbon	349	[21]

Table S3

Table S3. HER performance of this work compared with the previously reported TMSs, transition metal oxide/hydroxide and some Co-based materials in 1.0 M KOH.

Catalysts	Loading amount (mg/cm^2)/Collector	Overpotential (mV) @10 mA/cm^2	Ref.
rGO/CS/$(Co,Fe)_xP_y$	0.63/glassy carbon	180	**This work**
CoP/CSNSs	0.51/glassy carbon	251	[6]
$NiFe_2O_4$-NC	1.4/glassy carbon	300	[22]
Ce-$MnCo_2O_4$	0.20/glassy carbon	389	[23]
$NiCo_2O_4$	0.12/Ni foam	370	[24]
CoP NPs@GO	0.20/glassy carbon	300	[25]
$Ni_{2/3}Fe_{1/3}$-rGO	0.25/glassy carbon	553	[26]
NiFeLDH@Co_3O_4	--/coat on FTO	303	[27]
Co_3O_4/CuO	0.03/glassy carbon	288	[28]
PNC/Co	0.03/glassy carbon	289	[29]
$NiCo_2S_4$ NA/CC	4.0/coat on carbon cloth	263	[30]
Ni_2P	--/Ti foil	322	[31]
CoP/Perovskite	0.255/glassy carbon	209	[32]
FeP	0.72/electrodeposition on Ti foil	207	[33]
CoNiP	0.51/glassy carbon	229.3	[34]

References

[1] X. Dong, X. Jing, Y. Mu, Y. Yu, C. Miao, C. Meng, C. Huang, Y. Zhang, Rational design of double-sandwich-like C@Co,CoO/Co_2SiO_4/rGO architectures boost electrochemical performances of Co_2SiO_4 for energy storage devices, Chem. Eng. J. 431 (2022) 133277.

[2] X. Dong, Y. Zhang, Q. Chen, H. Jiang, Q. Wang, C. Meng, Z. Kou, Ammonia-etching-assisted nanotailoring of manganese silicate boosts faradaic capacity for high-performance hybrid supercapacitors, Sustain. Energy Fuels 4 (2020) 2220-2228.

[3] X. Dong, Y. Zhang, Q. Wang, X. Zhang, M. Gao, M. Changgong, Synthesis of urchin-like $Ni_3Si_2O_5(OH)_4$ hierarchical hollow spheres/GO composite with enhanced electrochemical properties for high-performance hybrid supercapacitors, Dalton Trans. 48 (2019) 11749-11762.

[4] X. Dong, Y. Yu, X. Jing, H. Jiang, T. Hu, C. Meng, C. Huang, Y. Zhang, Sandwich-like honeycomb Co_2SiO_4/rGO/honeycomb Co_2SiO_4 structures with enhanced electrochemical properties for high-performance hybrid supercapacitor, J. Power Sources 492 (2021) 229643.

[5] Y. Mu, X. Pei, Y. Zhao, X. Dong, Z. Kou, M. Cui, C. Meng, Y. Zhang, In situ confined vertical growth of $Co_{2.5}Ni_{0.5}Si_2O_5(OH)_4$ nanoarrays on rGO for an efficient oxygen evolution reaction, Nano Mater. Sci. 5 (2023) 351-360.

[6] Y. Mu, Y. Zhang, Z. Feng, X. Dong, X. Jing, X. Pei, Y. Zhao, Z. Kou, C. Meng, Bifunctional electrocatalyst junction engineering: CoP nanoparticles in-situ anchored on $Co_3(Si_2O_5)_2(OH)_2$ nanosheets for highly efficient water splitting, Chem. Eng. J. 460 (2023) 141709.

[7] Y. Zang, H. Zhang, X. Zhang, R. Liu, S. Liu, G. Wang, Y. Zhang, H. Zhao, Fe/Fe_2O_3 nanoparticles anchored on Fe-N-doped carbon nanosheets as bifunctional oxygen electrocatalysts for rechargeable zinc-air batteries, Nano Res. 9 (2016) 2123-2137.

[8] J. Yang, G. Zhu, Y. Liu, J. Xia, Z. Ji, X. Shen, S. Wu, Fe_3O_4-Decorated Co_9S_8Nanoparticles In Situ Grown on Reduced Graphene Oxide: A New and Efficient Electrocatalyst for Oxygen Evolution Reaction, Adv. Funct. Mater. 26 (2016) 4712-4721.

[9] Z. Luo, S. Marti-Sanchez, R. Nafria, G. Joshua, M. de la Mata, P. Guardia, C. Flox, C. Martinez-Boubeta, K. Simeonidis, J. Llorca, J.R. Morante, J. Arbiol, M. Ibanez, A. Cabot, Fe_3O_4@$NiFe_xO_y$ Nanoparticles with Enhanced Electrocatalytic Properties for Oxygen Evolution in Carbonate Electrolyte, ACS Appl. Mater. Interfaces 8 (2016) 29461-29469.

[10] T.Y. Ma, S. Dai, M. Jaroniec, S.Z. Qiao, Metal-organic framework derived hybrid Co_3O_4-carbon

porous nanowire arrays as reversible oxygen evolution electrodes, J. Am. Chem. Soc. 136 (2014) 13925-13931.

[11] Y. Wang, T. Zhou, K. Jiang, P. Da, Z. Peng, J. Tang, B. Kong, W.-B. Cai, Z. Yang, G. Zheng, Reduced Mesoporous Co3O4Nanowires as Efficient Water Oxidation Electrocatalysts and Supercapacitor Electrodes, Advanced Energy Materials 4 (2014).

[12] F. Shi, K. Huang, Y. Wang, W. Zhang, L. Li, X. Wang, S. Feng, Black Phosphorus-Modified Co_3O_4 through Tuning the Electronic Structure for Enhanced Oxygen Evolution Reaction, ACS Appl. Mater. Interfaces 11 (2019) 17459-17466.

[13] T. Zhou, W. Xu, N. Zhang, Z. Du, C. Zhong, W. Yan, H. Ju, W. Chu, H. Jiang, C. Wu, Y. Xie, Ultrathin Cobalt Oxide Layers as Electrocatalysts for High-Performance Flexible Zn-Air Batteries, Adv. Mater. 31 (2019) e1807468.

[14] K.-L. Yan, X. Shang, Z. Li, B. Dong, X. Li, W.-K. Gao, J.-Q. Chi, Y.-M. Chai, C.-G. Liu, Ternary mixed metal Fe-doped $NiCo_2O_4$ nanowires as efficient electrocatalysts for oxygen evolution reaction, Appl. Surf. Sci. 416 (2017) 371-378.

[15] J.F. Qin, J.Y. Xie, N. Wang, B. Dong, T.S. Chen, Z.Y. Lin, Z.Z. Liu, Y.N. Zhou, M. Yang, Y.M. Chai, Surface construction of loose $Co(OH)_2$ shell derived from ZIF-67 nanocube for efficient oxygen evolution, J. Colloid Interface Sci. 562 (2020) 279-286.

[16] F. Lyu, Y. Bai, Q. Wang, L. Wang, X. Zhang, Y. Yin, Phase-controllable synthesis of cobalt hydroxide for electrocatalytic oxygen evolution, Dalton Trans. 46 (2017) 10545-10548.

[17] S. Feng, C. Liu, Z. Chai, Q. Li, D. Xu, Cobalt-based hydroxide nanoparticles @ N-doping carbonic frameworks core–shell structures as highly efficient bifunctional electrocatalysts for oxygen evolution and oxygen reduction reactions, Nano Res. 11 (2018) 1482-1489.

[18] Y. Wang, Y. He, M. Zhou, Fabrication of hierarchical $Co(OH)_2$@$Ni(OH)_2$ core-shell nanosheets on carbon cloth as an advanced electrocatalyst for oxygen evolution reaction, Appl. Surf. Sci. 479 (2019) 1270-1276.

[19] M.-C. Sung, G.-H. Lee, D.-W. Kim, CeO_2/$Co(OH)_2$ hybrid electrocatalysts for efficient hydrogen and oxygen evolution reaction, J. Alloys Compd. 800 (2019) 450-455.

[20] C. Manjunatha, N. Srinivasa, S. Samriddhi, C. Vidya, S. Ashoka, Studies on anion-induced structural transformations of iron(III) (Hydr)oxide micro-nanostructures and their oxygen evolution reaction performance, Solid State Sci. 106 (2020).

[21] L. Yang, B. Zhang, W. Ma, Y. Du, X. Han, P. Xu, Pearson's principle-inspired strategy for the synthesis of amorphous transition metal hydroxide hollow nanocubes for electrocatalytic oxygen evolution, Mater. Chem. Front. 2 (2018) 1523-1528.

[22] N. Dalai, B. Mohanty, A. Mitra, B. Jena, Highly Active Ternary Nickel–Iron oxide as Bifunctional Catalyst for Electrochemical Water Splitting, ChemistrySelect 4 (2019) 7791-7796.

[23] X. Huang, H. Zheng, G. Lu, P. Wang, L. Xing, J. Wang, G. Wang, Enhanced Water Splitting Electrocatalysis over $MnCo_2O_4$ via Introduction of Suitable Ce Content, ACS Sustainable Chem. Eng. 7 (2018) 1169-1177.

[24] R. Elakkiya, R. Ramkumar, G. Maduraiveeran, Flower-like nickel-cobalt oxide nanomaterials as bi-functional catalyst for electrochemical water splitting, Materials Research Bulletin 116 (2019) 98-105.

[25] Z. Li, D. Wu, Y. Ouyang, H. Wu, M. Jiang, F. Wang, L.Y. Zhang, Synthesis of hollow cobalt phosphide nanocrystals with ultrathin shells anchored on reduced graphene oxide as an electrocatalyst toward hydrogen evolution, Appl. Surf. Sci. 506 (2020) 144975.

[26] W. Ma, R. Ma, C. Wang, J. Liang, X. Liu, K. Zhou, T. Sasaki, A Superlattice of Alternately Stacked Ni-Fe Hydroxide Nanosheets and Graphene for Efficient Splitting of Water, ACS Nano 9 (2015) 1977-1984.

[27] A. Tahira, Z.H. Ibupoto, M. Vagin, U. Aftab, M.I. Abro, M. Willander, O. Nur, An efficient bifunctional electrocatalyst based on a nickel iron layered double hydroxide functionalized Co_3O_4 core shell structure in alkaline media, Catal. Sci. Technol. 9 (2019) 2879-2887.

[28] A. Tahira, Z.H. Ibupoto, M. Willander, O. Nur, Advanced Co_3O_4–CuO nano-composite based electrocatalyst for efficient hydrogen evolution reaction in alkaline media, Int. J. Hydrogen Energy 44 (2019) 26148-26157.

[29] X. Li, Z. Niu, J. Jiang, L. Ai, Cobalt nanoparticles embedded in porous N-rich carbon as an efficient bifunctional electrocatalyst for water splitting, J. Mater. Chem. A 4 (2016) 3204-3209.

[30] D. Liu, Q. Lu, Y. Luo, X. Sun, A.M. Asiri, $NiCo_2S_4$ nanowires array as an efficient bifunctional electrocatalyst for full water splitting with superior activity, Nanoscale 7 (2015) 15122-15126.

[31] Z. Zhou, L. Wei, Y. Wang, H.E. Karahan, Z. Chen, Y. Lei, X. Chen, S. Zhai, X. Liao, Y. Chen, Hydrogen evolution reaction activity of nickel phosphide is highly sensitive to electrolyte pH, J. Mater. Chem. A 5 (2017) 20390-20397.

[32] Y.-Q. Zhang, H.-B. Tao, Z. Chen, M. Li, Y.-F. Sun, B. Hua, J.-L. Luo, In situ grown cobalt phosphide (CoP) on perovskite nanofibers as an optimized trifunctional electrocatalyst for Zn–air batteries and overall

water splitting, J. Mater. Chem. A 7 (2019) 26607-26617.

[33] L. Tian, X. Yan, X. Chen, Electrochemical Activity of Iron Phosphide Nanoparticles in Hydrogen Evolution Reaction, ACS Catal. 6 (2016) 5441-5448.

[34] Y. Du, M. Zhang, Z. Wang, Y. Liu, Y. Liu, Y. Geng, L. Wang, A self-templating method for metal–organic frameworks to construct multi-shelled bimetallic phosphide hollow microspheres as highly efficient electrocatalysts for hydrogen evolution reaction, J. Mater. Chem. A 7 (2019) 8602-8608.